Three-dimensional finite element modelling of laser surface modification

M Labudovic, D Hu and **R Kovacevic***
Department of Mechanical Engineering, Southern Methodist University, Dallas, Texas, USA

Abstract: A three-dimensional finite element modelling of laser surface modification is presented. The design capabilities of the ANSYS parametric design language (APDL) were employed for this purpose. The model calculates transient temperature profiles and the dimensions of fusion and the heat-affected zone (HAZ). Model simulations are compared with experimental results, acquired on-line using an ultra-high shutter speed camera which is able to acquire well-contrasted images of the molten pool, and off-line, using metallographical analysis, that show very good agreement. The results are further discussed to provide directions for feedback and process control.

Keywords: laser surface modification, finite element modelling, Nd:YAG laser, image processing

NOTATION

c	specific heat capacity (J/kg K)
$[\boldsymbol{C}]$	specific heat (or capacitance) matrix
h	heat transfer coefficient for convection (W/m^2 K)
k_n	thermal conductivity normal to S_2 (W/m K)
k_x, k_y, k_z	thermal conductivity in the x, y and z directions respectively (W/m K)
$[\mathbf{K}]$	conductivity matrix
q	heat flux normal to S_2 (W/m^2)
Q	power generation per unit volume in domain D (W/m^3)
$\{\boldsymbol{Q}\}$	nodal heat flow vector
t	time (s)
T_0	ambient temperature (K)
$\{\boldsymbol{T}\}$	vector of nodal temperatures
$\{\dot{\boldsymbol{T}}\}$	vector of time derivative of $\{\boldsymbol{T}\}$
v	velocity of the moving heat source (m/s)
$\{\boldsymbol{V}\}$	velocity vector for moving laser beam
(x, y, z)	coordinate system attached to heat source
ε	emissivity
ρ	density (kg/m^3)
σ	Stefan–Boltzmann constant for radiation (5.67×10^{-8} $W/m^2 K^4$)

The MS was received on 6 July 1999 and was accepted after revision for publication on 3 December 1999.
**Corresponding author: Department of Mechanical Engineering, Southern Methodist University, PO Box 750337, Dallas, TX 75275, USA.*

1 INTRODUCTION

Laser surface treatments comprise a family of processes such as transformation hardening, melting, alloying and cladding. It allows one to build a part with completely different properties in the surface layer from the bulk material. In such a way, the surface layer can achieve high wear, fatigue or corrosion resistance while the bulk material can still keep its original properties.

The mechanisms involved in the most common laser surface treatments are summarized in Fig. 1. The first stage of all laser treatments is the absorption of laser radiation in the substrate. Absorption occurs in a very thin surface layer, where the optical laser energy is converted to heat. The absorbed heat diffuses into the surrounding bulk material by conduction. The effects of laser remelting and laser transformation hardening are based on microstructural changes of the surface layer. However, if the base material cannot be improved sufficiently, it can be necessary, or cheaper, to apply a layer with a different composition on top of the base material. Three laser techniques that can enhance surface properties by changing the material composition in the surface can be distinguished: laser alloying, laser surface modification and laser cladding. All three methods involve the formation of a molten pool to which material is applied.

The positive effects of laser surface treatments are based on a change of the microstructure of the material composition of the surface layer due to a thermal cycle which is induced by a moving laser source. The treated area is heated by absorption of energy delivered by the laser beam. Since the heat input is by a high power

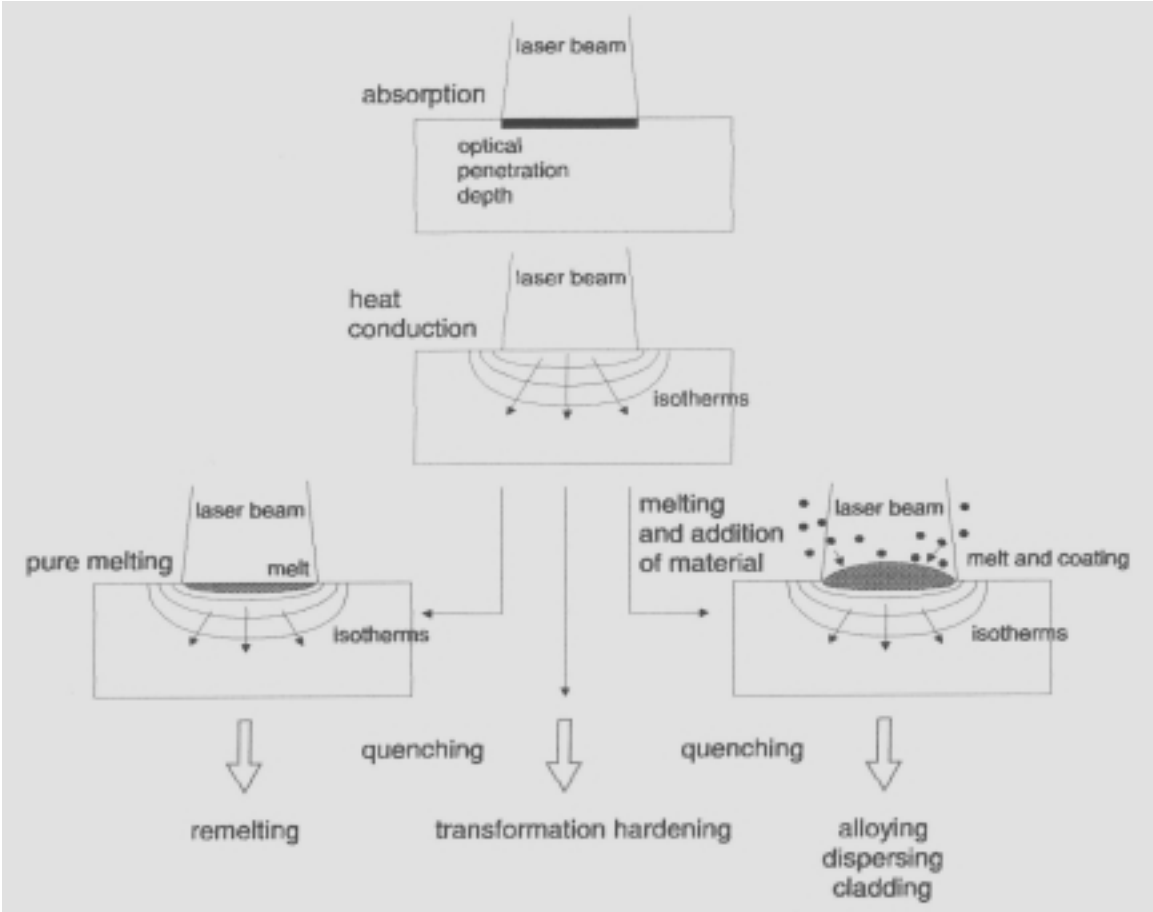

Fig. 1 Basic mechanisms involved in laser surface treatments

laser beam it is well confined and very intense. Hence, heating rates in the surface layer are high. The heated layer is self-quenched, after the laser beam passes, by diffusion of the heat to the cold bulk. The high heating and cooling rates in the surface layer result in grain refinement and in the formation of metastable phases and/or altered microstructures. Thus, to achieve an acceptable temperature distribution, the heat input by the laser source must be very well controlled.

The laser beam can be considered as a moving heat source with a certain power density distribution that imposes a boundary condition on the substrate surface. The classical approach to modelling the heat flow induced by a distributed heat source moving over the surface of semi-infinite solid starts with the solution of the heat diffusion equation to determine a point source [**1**]. Following the classical analysis of temperature variations resulting from moving heat sources by Rosenthal [**2**], a number of studies have added realistic effects, such as temperature-dependent material properties and radiative and convective boundary conditions, on the workpiece surface. Also, instead of the idealized point and line source variations, closer approximations to the heat inputs, including Gaussian and more complex profiles, have been examined. Many of these efforts have been summarized by Goldak *et al.* and Mahin *et al.* [**3–5**].

A completely general three-dimensional model of the laser surface modification processes is not currently available. As indicated by Giedt [**6**], a simpler simulation, which accommodates for the molten pool convection only empirically, may be adequate for many automation applications requiring real-time process monitoring and control. Automated systems are currently being investigated for laser processing of several materials (e.g. high-strength, low-alloy steels). The vision system is used in laser processing for process monitoring and for detecting any deviations from ideal conditions due to various anomalies. Real-time process correction may be provided by comparing the measured signal with that predicted by a model. While limited experiments on seam tracking and cooling rate control using surface temperature sensing have been reported [**7**], no general numerical models appear to have been developed to supplement these experiments.

This paper presents a new three-dimensional model of the laser surface modification process utilizing the efficient solution procedures of the finite element capabilities of the ANSYS parametric design language (APDL). The results of the model are compared with experimental

results. A high-power Nd:YAG laser of wavelength 1.06 μm operating in continuous wave (CW) mode was used to generate single modified surfaces on type AISI 1006 steel plates. An ultra-high speed shutter camera with pulsed laser illumination has been used as the laser process detector, which is able to acquire well contrasted images of the molten pool. The physical dimensions of the fusion zone (FZ) and heat-affected zone (HAZ) were measured and compared with the predictions of the model.

Since the geometrical features of the molten pool can be used as an effective feedback to estimate the molten depth, a model was built to explore the correlation between molten depth, molten pool geometry and processing parameters (laser power and scanning speed).

2 PHYSICAL DESCRIPTION OF THE MODEL

The following assumptions were made in the formulation of the finite element model:

1. The laser beam is incident at an angle θ to the surface of the workpiece in order to prevent back-reflections from the workpiece.
2. The workpiece is initially at 298 K. Both the workpiece and the coordinate mesh are fixed and the laser beam moves in the positive z direction with a constant velocity, v.
3. The transverse electromagnetic mode (TEM) of the laser beam is neglected and simplified to uniform one, although the laser beam can be TEM_{00}, TEM_{01}, TEM_{10}, TEM_{11} and TEM_{20} or their combinations.
4. All thermophysical properties are considered to be temperature dependent. These properties are shown in Table 1 [**8**, **9**].
5. The latent heat of fusion is simulated by an artificial increase in the liquid specific heat according to Brown and Song [**8**] (and as included in Table 1) and the relationship between the enthalpy, density and specific heat

$$H = \int \rho c(T)\,\mathrm{d}t \tag{1}$$

6. The absorption of the Nd: YAG laser light by the metal is assumed to be 30 per cent [**10**].
7. Since laser surface modification involves very rapid melting and solidification, convective redistribution of heat within the molten pool is not significant (it is in other processes where a liquid pool is permanent). Convective flow of heat, therefore, is neglected.
8. Since the laser is defocused, there is no keyhole formation and the energy absorption of the plasma can be neglected.

Table 1 Thermophysical properties used in the finite element model

Temperature (°C)	Thermal conductivity (W/m K)	Specific heat (J/kg K)	Emissivity	Density (kg/m^3)
0	51.9	450	0.2	7872
75	51.3	486	0.35	7852
100	51.1	494	0.4	7845
175	49.5	519	0.44	7824
200	49	526	0.45	7816
225	48.3	532	0.46	7809
275	46.8	557	0.47	7763
300	46.1	566	0.48	7740
325	45.3	574	0.5	7717
375	43.6	599	0.51	7727
400	42.7	615	0.53	7733
475	40.2	662	0.54	7720
500	39.4	684	0.55	7711
575	36.6	749	0.56	7680
600	35.6	773	0.57	7669
675	32.8	846	0.57	7636
700	31.8	1139	0.58	7625
730	30.1	1384	0.58	7612
750	28.9	1191	0.58	7602
775	27.5	950	0.58	7590
800	26	931	0.59	7578
1000	27.2	779	0.6	7552
1500	29.7	400	0.6	7268
1540	29.7	400	0.6	7218
1590	29.7	847	0.6	7055
1840	29.7	847	0.6	6757
1890	29.7	400	0.6	6715
2860	29.7	400	0.62	5902

3 MATHEMATICAL DESCRIPTION OF THE MODEL

The transient temperature distribution $T(x, y, z, t)$ satisfies the following differential equation for three-dimensional heat conduction in a D domain:

$$\frac{\partial}{\partial x}\left(k_x \frac{\partial T}{\partial x}\right) + \frac{\partial}{\partial y}\left(k_y \frac{\partial T}{\partial y}\right) + \frac{\partial}{\partial x}\left(k_z \frac{\partial T}{\partial z}\right) + Q = \rho c\left(\frac{\partial T}{\partial t} - v\frac{\partial T}{\partial x}\right) \tag{2}$$

The initial condition is

$$T(x, y, z, 0) = T_0 \qquad \text{for } (x, y, z) \in D \tag{3}$$

The essential boundary condition is

$$T(0, x, z) = T_0 \tag{4}$$

on the boundary S_1 for $(x, z) \in S_1$ and $t > 0$. S_1 represents the bottom surface of the plate.

The natural boundary conditions can be defined by

$$k_n \frac{\partial T}{\partial n} - q + h(T - T_0) + \sigma\varepsilon(T^4 - T_0^4) = 0 \tag{5}$$

on the boundary S_2 for $(x, y, z) \in S_2$ and $t > 0$. S_2 represents those surfaces that are subjected to radiation, convection and imposed heat fluxes.

The inclusion of temperature-dependent thermophysical properties and a radiation term in the above boundary condition makes this type of analysis highly nonlinear. Since the incorporation of radiation effects is found to increase the solution by as much as three times, Vinokurov's [**11**] empirical relationship for welding hot-rolled steel plates was used

$$H = 2.4 \times 10^{-3} \varepsilon T^{1.61} \tag{6}$$

Equation (6) combines the effect of radiation and convection into a 'lumped' heat transfer coefficient. The associated loss in accuracy using this relationship is estimated to be less than 5 per cent [**12**].

4 NUMERICAL DESCRIPTION OF THE MODEL

ANSYS provides a convenient means of numerically modelling laser surface modification processes. This requires an integration of the heat conduction equation with respect to time. In the finite element formulation, this equation can be written for each element as

$$[\mathbf{C}(T)]\{\boldsymbol{T}\} + [\mathbf{K}(T)]\{\boldsymbol{T}\} + \{\boldsymbol{V}\} = \{\boldsymbol{Q}(T)\} \tag{7}$$

The moving laser beam is simulated using ANSYS parametric design language (APDL) to provide the heat boundary conditions at different positions at different times.

The first iteration in the solution procedure solves the system equations at an assumed starting temperature (298 K), and subsequent iterations use temperatures from previous iterations to calculate thermal conductivity and specific heat matrices. The iterative process continues for time period T until a converged solution is achieved or until the dynamic equilibrium of heat exchanging is established. Based on the image analysis of the molten pool performed in Section 3, it is concluded that the geometric shape of the molten pool will be in steady state after 2 s. Therefore, $T = 2$ s is used as the time period T once dynamic equilibrium has been established for the heat exchanging.

The solution data are in the form of nodal temperatures and heat flows. The results can be post processed by a time history post-processor and displayed in graphical or tabular form.

5 EXPERIMENT

The experimental set-up that consists of an Nd:YAG laser, two-axis CNC positioning system, laser strobe vision system, shielding gas and workpiece is shown in Fig. 2. Fibre optics conducts a laser light of wavelength 337 nm to illuminate the Nd:YAG laser treating area. The illuminating laser is a nitrogen pulse laser with 5 ns pulse duration synchronizing with the high-speed shutter of the camera. The camera of the laser strobe vision system is equipped with an ultraviolet (UV) filter that only allows light of about 337 nm wavelength to pass. During the illumination period, the intensity of the illuminating laser can suppress the spatter and plasma light. In addition, due to the reflection of the mirror-like molten pool, a well contrasted image of the molten pool can be obtained. Nitrogen is used as an alloying gas and as a shielding gas.

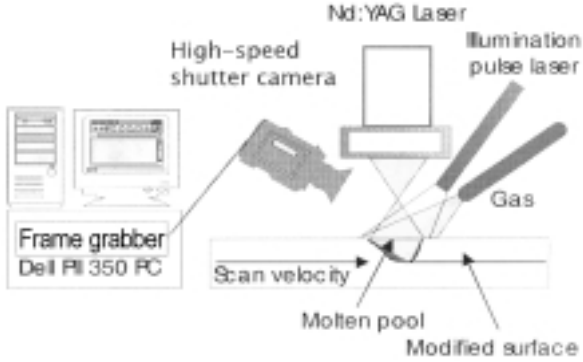

Fig. 2 Experimental set-up

A frame grabber installed on a PII 350 PC computer acquires images from the ultra-high shutter speed camera at 30 Hz. Real-time image processing and recognition, as well as molten depth estimation and closed-loop control, will be completed on the same computer.

6 RESULTS AND DISCUSSION

6.1 Real-time algorithm for edge detection

In order to extract the geometrical features of the molten pool, an edge detection algorithm must first be developed. The geometrical features extracted by the image processing algorithm will then be used for comparison with those developed by the finite element model.

Edge detection serves to simplify the analysis of the image by preserving useful structural information about the object boundaries. There are several research results on edge detection (well known ones include Canny, Nalwa–Binford, Sarkar–Boyer and Sobel [**13**]). Due to the excellent performance of the Canny edge detector (high signal–noise ratio, good edge localization and elimination of multiple response) and the features of the images that were obtained, the Canny edge detector for step-edge is used, with modification, to serve as the front-end edge detector.

In order to decrease the noise effects, Gaussian smoothing is applied to the image first described as follows:

$$I_s = G * I \tag{8}$$

where G is a two-dimension Gaussian filter, I represents

a) b) c)

Fig. 3 Processing results of the edge detector: (a) original image acquired by high shutter speed camera, (b) intermediate processing result of edge detector, (c) final processing result of edge detector

the image array and $*$ denotes convolution:

$$G = \exp\left(-\frac{x^2 + y^2}{2\sigma^2}\right) \tag{9}$$

According to Canny [**13**], the first derivative of the Gaussian operator is an efficient approximation to the optimized operator for step-edge with a 20 per cent decrease in performance. Thus, the following operation is applied to the smoothed image:

$$I_r = G_n I_s \tag{10}$$

where

$$G_n = \frac{\partial G}{\partial n} = n\,\nabla G \tag{11}$$

n should be the normal to the direction of an edge to be detected and can be estimated from the smoothed gradient direction

$$n = \frac{\nabla(G \quad I)}{|\nabla(G \quad I)|} \tag{12}$$

An edge candidate I_e is a local maximum of I_r. A function (F) of non-maximum suppression is built to substitute for calculating the second derivation Gaussian operator:

$$I_e = F(I_r) \tag{13}$$

Two edge magnitude thresholds, T_{e1} and T_{e2} ($T_{e1} > T_{e2}$), are selected with hysteresis [**13**] to classify I_e and to form the edge set E. Figure 3a shows the original image of the molten pool as acquired by high shutter speed camera, while Fig. 3b shows the results of the image processing.

In order to eliminate the edges caused by the heat-affected zone, two grey level thresholds, T_{g1} and T_{g2}

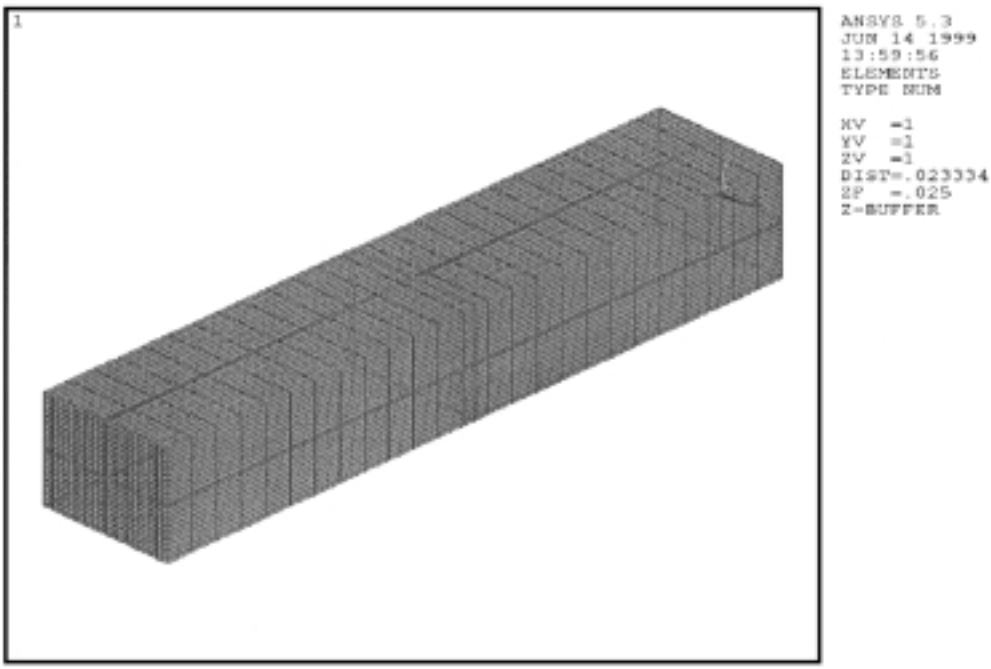

Fig. 4 Finite element mesh for ANSYS analysis

($T_{g1} < T_{g2}$), also with hysteresis, are used combined with edge magnitude thresholds, based on the original image histogram analysis. The process is defined as follows:

If $I_e(x, y) > T_{e1}$ and $I(x, y) < T_{g1}$, $(x, y) \in E$, break = FALSE, $x \pm \Delta$, $y \pm \Delta$; Δ is a small increase
If $I_e(x, y) < T_{e2}$ or $I(x, y) > T_{g2}$, $(x, y) \notin E$, break = TRUE
If $T_{e1} > I_e(x, y) > T_{e2}$ and $T_{g2} > I(x, y) > T_{g1}$ and break = FALSE, $(x, y) \in E$, otherwise break = TRUE

Figure 3c shows that the extra edges are greatly reduced. The edge set E is the data source of the next step recognition.

6.2 Comparison of the experimental and modelling results

The comparison of experimental with simulated results may allow the estimation of the relative importance and role of the complex physical interactions that govern laser surface modification processes. The

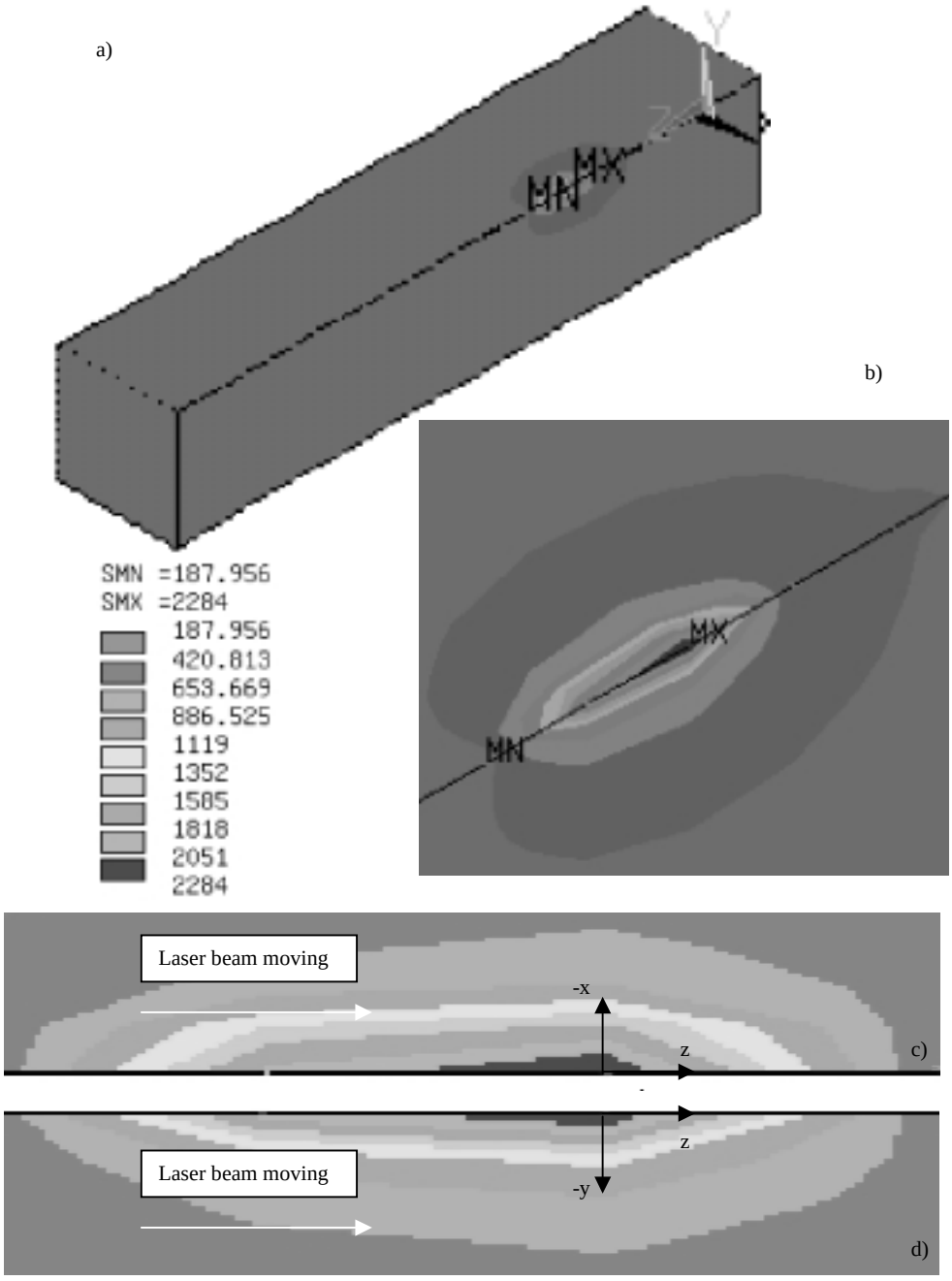

Fig. 5 Graphic display of analysis results (laser power = 300 W, scanning speed = 5 mm/s): (a) overview, (b) zoom view, (c) top view and (d) right view

comparison of experiment and simulation was done on a type AISI 1006 steel plate with dimensions $20 \times 10 \times 50$ mm. The finite element mesh is shown in Fig. 4. Because of symmetry about the *zy* plane, only half of the plate is considered. The model was run for both the duration of the laser heating and for the subsequent cooling period using different powers (in the range 300–1200 W), and scanning speeds (in the range 2.5–10 mm/s). Figure 5 shows the typical analysis resulting from the use of a scanning speed of 5 mm/s and 300 W laser power.

The data generated during the solution procedure includes depth of the 1540 and 730 °C isotherms that approximately represent the fusion zone (FZ) and heat-affected zone (HAZ) boundaries, respectively. These data are then compared with experimental results. Figures 6 and 7 show micrographs of the cross-sections of two modified surfaces (laser power 300 W and scanning speeds of 5 and 2.5 mm/s respectively). The depth and width of the FZ and HAZ may be measured from these micrographs. Just as this laser-modified surface was physically sectioned, a section through the centreline of the model can also be taken. ANSYS model predictions of the FZ and HAZ are superimposed on these micrographs. These isotherms represent the positions that have been heated to a maximum temperature of 1540 and 730 °C respectively.

The model was also run for the other laser powers and scanning speeds. The temperature of each nodal point within the solid was calculated as a function of time. The maximum depth and diameter of the 1540 and 730 °C temperature contours were measured for each laser power and scanning speed. These measurements have been plotted in Fig. 8, and may be compared directly with the experimental measurements of the FZ and HAZ dimensions respectively.

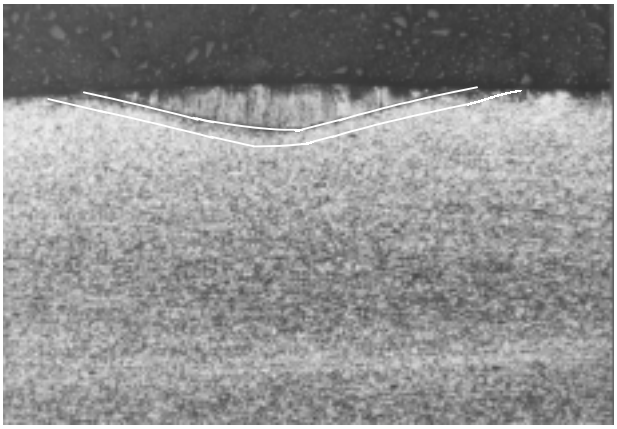

Fig. 6 Micrograph of the cross-section of a modified surface showing model predictions of the fusion and heat-affected zone boundaries (laser power = 300 W, scanning speed = 5 mm/s)

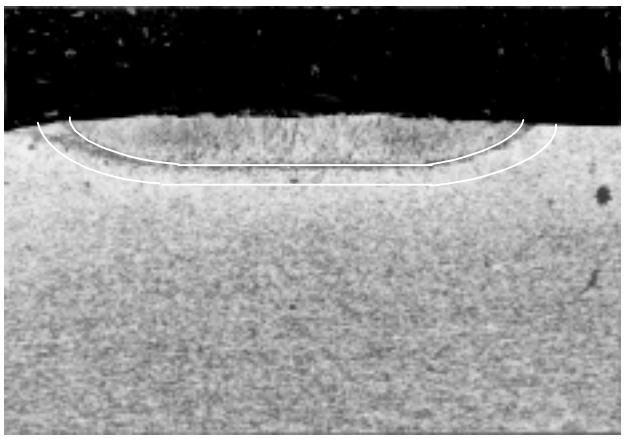

Fig. 7 Micrograph of the cross-section of a modified surface showing model predictions of the fusion and heat-affected zone boundaries (laser power = 300 W, scanning speed = 2.5 mm/s)

The isotherms corresponding to the 1540 °C are superimposed on the images of the molten pool acquired on-line by a laser strobe vision system (Fig. 9). They show very good agreement between the simulated results and the results obtained by an image processing algorithm developed in Section 3 for validation. The size and shape of the molten region obtained on-line is almost the same as those obtained by simulation for all applied laser powers and scanning speeds. In addition, by observing the molten pool it can be seen that the pool is deeper at the end than at the front because of the accumulation of heat. However, an increase of the laser power and decrease of the scanning speed resulted in a wider molten pool. The display of these distinct characteristic signatures on the surface temperature patterns allows the depth of the molten pool to be estimated, which is the major issue of the recent trend towards surface modification automation. Therefore, since there are no reliable sensors presently available for the remote, real-time measurement of absolute molten pool temperature, the obtained results can be used for molten pool depth estimation and closed-loop control of the laser surface modification. The real-time control of the process, in order to produce more stable and repeatable molten pool depth and adaptation of the model to a more complex shape of the processed parts, will be a challenge in subsequent research.

7 CONCLUSIONS

A three-dimensional finite element model of the heat flow during laser surface modification has been developed. The simulation and experimental results are in very good agreement with each other.

For example, simulation results provide a cross-sectional shape of the molten pool that cannot be

observed during real-time processing. From such sections, the depths of the FZ and HAZ are measured and then compared with those obtained metallographically by actual physical sectioning of the specimens. The results have shown that the depths of the FZ and HAZ obtained by modelling coincide with those obtained by metallographical analysis, for different processing parameters (laser powers and scanning speeds).

In addition, the results are certified by the top-side image of the molten pool acquired on-line by the high shutter speed camera. Again, the shape of the molten

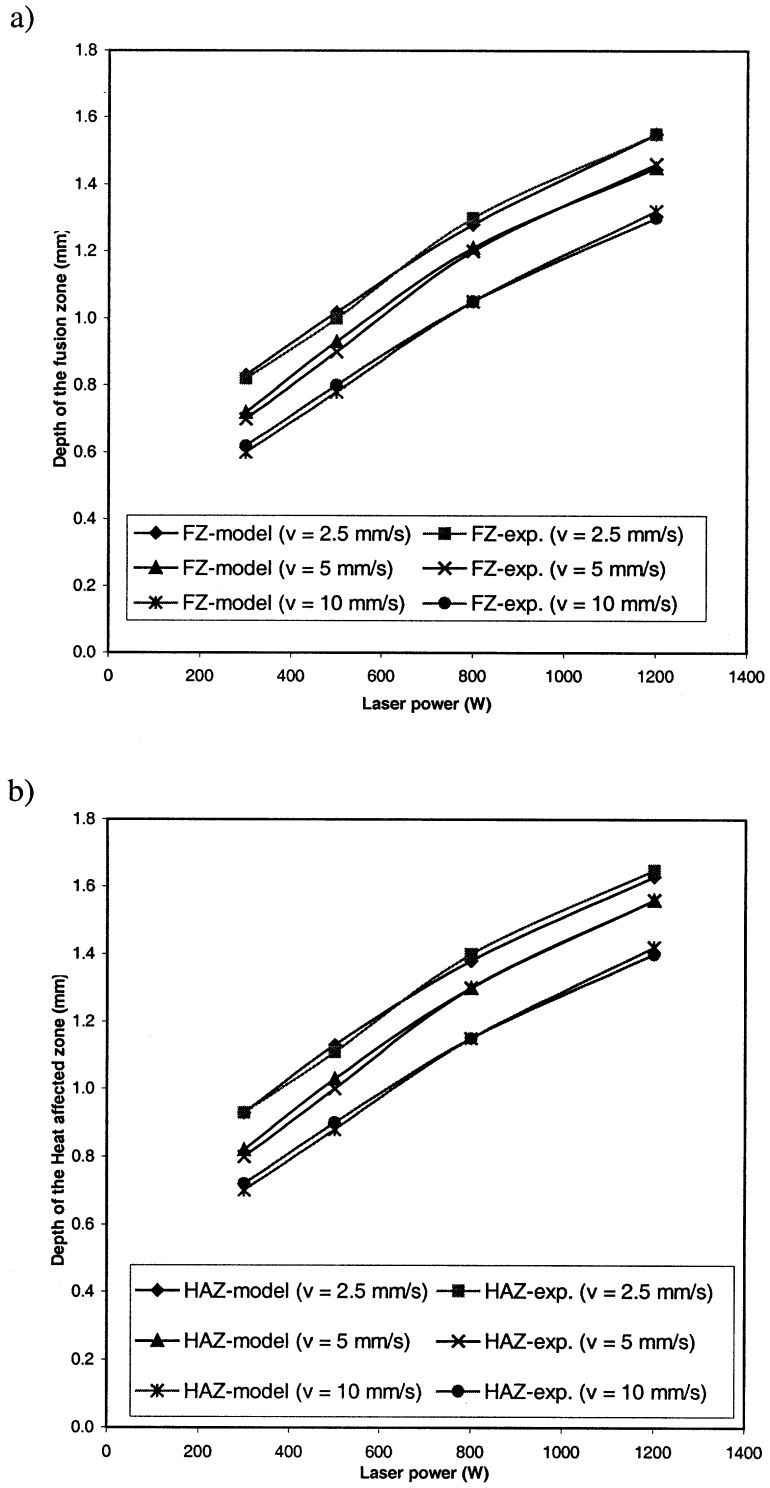

Fig. 8 Measured: (a) FZ and (b) HAZ depths compared with model predictions for different laser powers and scanning speeds

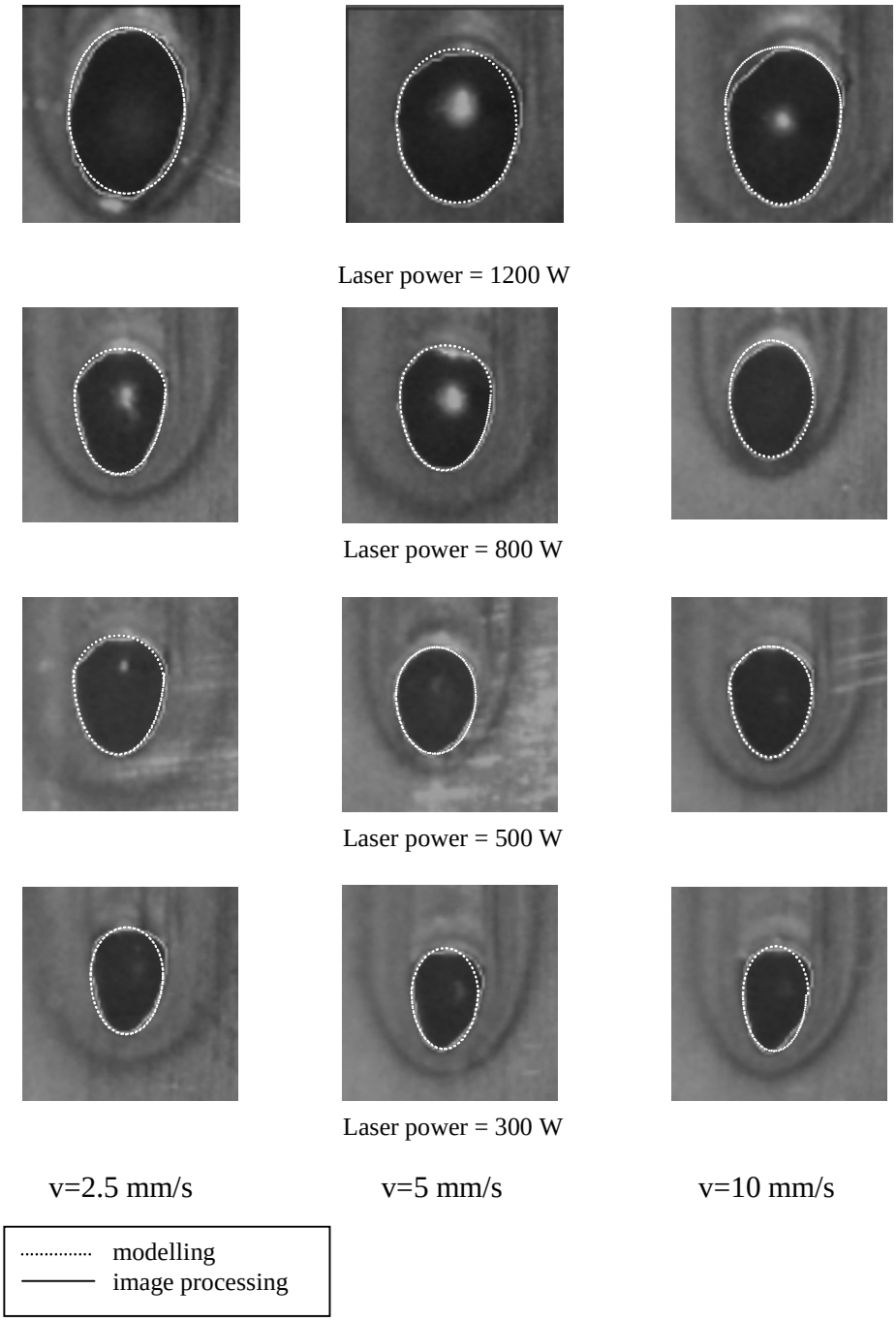

Fig. 9 Comparison of the FZ boundaries acquired on-line by a high-speed shutter camera with those obtained by the model

pool obtained by the modelling coincides with that obtained by image processing, for different processing parameters (laser powers and scanning speeds). The pool is deeper at the end than at the beginning of the bead because of the heat accumulation. In reality, this means that relationships exist between the shape and depth of the molten pool. Therefore, a capability to computationally predict the FZ and HAZ boundaries allows the possibility of a surface modification monitoring system based on temperature sensing and machine vision to be constructed.

REFERENCES

1 **Ule, R. L., Joshi, Y.** and **Sedy, E. B.** A new technique for three-dimensional transient heat transfer computations of autogenous arc welding. *Metall. Trans. B, Process Metall.*, 1990, **21B**, 1033–1047.

2 **Rosenthal, D.** The theory of moving sources of heat and its application to heat transfer. *Trans. ASME*, 1946, **68**, 849–866.

3 **Goldak, J., McDill, M., Oddy, A., House, R., Chi, X.** and **Bibby, M.** Computational heat transfer for welding mechanics. Advances in welding science and technology. In Proceedings of International Conference on *Trends in Welding Research* (*TWR '86*), Gatlinburg, Tennessee, 1986, pp. 15–20 (ASM International, Metals Park, Ohio).

4 **Mahin, K. W., Shapiro, A. B.** and **Hallquist, J.** Assessment of boundary condition limitations on the development of a general computer model for fusion welding. Advances in welding science and technology. In Proceedings of International Conference on *Trends in Welding Research* (*TWR '86*), Gatlinburg, Tennessee, 1986, pp. 215–223 (ASM International, Metals Park, Ohio).

5 **Goldak, J.** Finite element method for welding heat sources. In Proceedings of International Conference on *Trends in Welding Technology* (Ed. S. A. David), Gatlinburg, Tennessee, 1989.

6 **Giedt, W. H.** Welding—an interdisciplinary science and technology. Interdisciplinary issues in material processing and manufacturing. In Proceedings of the Winter Annual Meeting of ASME, Boston, Massachusetts, 1987, pp. 45–57.

7 **Lukens, W. E.** and **Morris, R. A.** Infrared temperature sensing of cooling rates for arc welding control. *Weld. J.*, 1982, **61**, 27–33.

8 **Brown, S.** and **Song, H.** Finite element simulation of welding of large structures. *J. Engng Industry*, 1992, **114**, 441–451.

9 **Kim, C. S.** Thermophysical properties of stainless steels. Technical Report ANL-75-55, Argonne National Laboratory, Argonne, 1975, pp. 1–24.

10 **Kou, S.** *Welding Metallurgy*, 1987, p. 33 (John Wiley, New York).

11 **Vinokurov, V. A.** *Welding Stresses and Distortion*, 1987, pp. 118–119 (Springer-Verlag, London).

12 **Frewin, M. R.** and **Scott, D. A.** Finite element model of pulsed laser welding. *Weld. J.*, 1999, **78**, 15–22.

13 **Canny, J.** A computational approach to edge detector. *IEEE Trans., Pattern Analysis Mach. Intell.*, 1986, **8**, 679–698.

